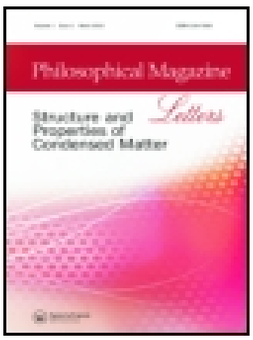

Taylor & Francis
Taylor & Francis Group

Philosophical Magazine Letters

ISSN: 0950-0839 (Print) 1362-3036 (Online) Journal homepage: https://www.tandfonline.com/loi/tphl20

Statistical modelling of microsegregation in laser powder-bed fusion

Supriyo Ghosh, Raiyan Seede, Jaylen James, Ibrahim Karaman, Alaa Elwany, Douglas Allaire & Raymundo Arroyave

To cite this article: Supriyo Ghosh, Raiyan Seede, Jaylen James, Ibrahim Karaman, Alaa Elwany, Douglas Allaire & Raymundo Arroyave (2020): Statistical modelling of microsegregation in laser powder-bed fusion, Philosophical Magazine Letters

To link to this article: https://doi.org/10.1080/09500839.2020.1753894

Published online: 27 Apr 2020.

PHILOSOPHICAL MAGAZINE LETTERS
https://doi.org/10.1080/09500839.2020.1753894

Taylor & Francis
Taylor & Francis Group

Statistical modelling of microsegregation in laser powder-bed fusion

Supriyo Ghosh [a]*, Raiyan Seede[a], Jaylen James[a], Ibrahim Karaman [a], Alaa Elwany[b], Douglas Allaire[c] and Raymundo Arroyave [a,b,c]

[a]Department of Materials Science & Engineering, Texas A&M University, College Station, TX, USA; [b]Department of Industrial & Systems Engineering, Texas A&M University, College Station, TX, USA; [c]Department of Mechanical Engineering, Texas A&M University, College Station, TX, USA

ABSTRACT

Laser powder-bed fusion solidification of Ni–Nb alloys often results in cellular morphology in which the solute microsegregation was determined using experiments and simulations, and the data obtained were utilised to explore the predictive capability of microsegregation models. The experimental 'ground truth' was compared with high-fidelity phase-field simulations as well as with analytical model predictions. Supervised statistical analyses, including linear regression, polynomial regression, and model reification were employed to understand the merit of these approaches toward microsegregation estimation. The bias-variance and accuracy-interpretability trade-off limits were considered in the data analysis that was consistent with our experimental findings.

ARTICLE HISTORY
Received 21 October 2019
Accepted 31 March 2020

KEYWORDS
Additive manufacturing; microsegregation; phase-field; regression; reification

1. Introduction

Laser powder-bed fusion (LPBF) metal additive manufacturing (AM) process has significant advantages over traditional manufacturing and metal forming routes [1–5]. Some of these advantages include design freedom for printing arbitrary shapes, improved material properties, minimal residual waste, and high economy-to-cost ratio [1–5]. The primary beneficiaries of AM processes are the aerospace and automobile sectors [1,4,6,7]. Ni-based superalloys, Ti–6Al–4V, Al–10Si–Mg, and steels are some of the metallic alloys that are printed widely *via* AM routes [1–8].

However, the full realisation of the potential of AM processes is impeded by uncertainty regarding the reliability of the final material in service [5,7,9–11]. Some 47% of manufacturers surveyed indicated that the uncertain quality of the final product was a barrier to the adoption of AM [12]. This is primarily due to rapid heating and cooling during the microstructure formation processes,

CONTACT Supriyo Ghosh supriyo.ghosh@lanl.gov, gsupriyo2004@gmail.com Department of Materials Science & Engineering, Texas A&M University, College Station, TX 77843, USA
*Present address: Los Alamos National Laboratory, Los Alamos, NM 87545, USA.

leading to significant variations and distributions of the key microstructural features, and eventually uneven qualities of the final product [3,5,7,13]. Therefore, microstructural evolution during AM processes is a critical stage that needs to be assessed thoroughly. The typical morphology that often forms during laser melting solidification processes is cellular in nature [1–4,8]. The key features in a cellular microstructure that determine the properties of the final material, particularly tensile strength and low-cycle fatigue life, are cellular spacing, microsegregation, and the misorientation between cells [5,8,14]. We refer to these microstructural features as the Quantities of Interest (QoIs) critical for material properties and behaviour in service. Let us consider microsegregation for our present measurements and analysis. Microsegregation results due to solute redistribution between the solid cell core and advancing solidification front in the solidifying alloy melt-pool [15–18]. We use Ni–Nb as the sample alloy material. Ni–Nb alloys show excellent mechanical properties and creep resistance at elevated temperatures and thus are often used in gas-turbine and jet-engine components [19]. Also, Ni–Nb is the most important binary analogue of Ni-based superalloys because Nb segregates most severely due to its smallest equilibrium partition coefficient among all the elements in the superalloy, controlling the average solidification behaviour of the material [19,20]. The as-solidified microstructures are further manipulated using appropriate post-deposition heat treatment schedules to homogenise the variation and distribution of the QoIs for property and performance control [3,8,21].

Modelling and simulation can accurately predict microstructure QoIs in a solidified melt-pool [22–24]. The phase-field (PF) method has become a powerful technique for simulating complex AM microstructures [15,24–29]. The PF method represents the microstructure phases and interfaces using single or multiple order parameter values to avoid explicit interface tracking and can be simulated efficiently using massively parallel computer architectures (for reviews, see [30–33]). We use PF simulations to simulate solidification microstructures that arise for local thermal gradient (G) and growth rate (V) conditions in the solidifying Ni–Nb melt pool. These local conditions are predicted by macroscale melt-pool simulations using finite element analysis (FEA) [34,35]. Besides FEA–PF simulations, the analytical model of Kurz and Fisher (KF) [17] was also considered to predict microsegregation. The emerging machine learning (ML) and statistical analysis (SA) methods [36,37] including regression and classification techniques [38,39] were further employed to analyse the microsegregation data obtained from the above numerical schemes.

Identifying key sensitive process and material parameters is the basis to understand and model the microstructure QoIs in reasonably accurate and interpretable ways [40–42]. A statistical data analysis is used for this purpose in which the variability of model inputs in terms of bias and variance contributions on microsegregation were modelled. In addition to the statistical schemes derived from PF, KF, and ML means, an information fusion or

reification [43] across multiple models was also performed for a more accurate estimation of microsegregation. In what follows, we first describe the LPBF experiments that represent the 'ground truth' for microsegregation. These measurements are then compared with simulations conducted with comparable solidification conditions, followed by suitable regression and reification analyses to model and approximate AM microsegregation.

2. Single-track experiments

Single-track LPBF experiments were carried out to approximate the 'ground truth' for microsegregation using a 3D Systems ProX DMP 200 printer (fibre laser with a Gaussian power distribution of wavelength 1070 nm and laser beam size of 100 μm. A Ni-5 wt% Nb alloy, provided by Nanoval GmbH & Co., was used as the powder as well as the substrate material. Various combinations of laser power and scan speed values were used with a laser scan length of 10 mm and 1 mm distance between the tracks. After the printing process, cross-sections of the single-tracks were cut using wire electrical discharge machining (EDM) and polished to 0.25 μm thickness using water-based diamond suspension solutions. Kalling's No. 2 solution (5 g $CuCl_2$, 100 ml HCl, and 100 ml ethanol) was used to etch the printed Ni–Nb tracks to reveal the optical microstructures under a Keyence VH-X digital microscope that was equipped with VH-Z100 wide-range zoom lens. Scanning electron microscopy (SEM) and wavelength dispersive spectroscopy (WDS) analyses were performed with a CAMECA SXFive electron probe microanalyser that was equipped with a LaB_6 electron source. Quantitative WDS composition maps were obtained with a nominal setting of 15 kV, 100 nA, and 110 μs pixel dwell time with a 0.1 μm step size. The WDS composition maps were analysed further to extract the elemental distribution within the solidification morphology.

The optical microscope reveals the solidified melt pool shape and boundary for different laser parameters (Figure 1(a)), and the SEM analysis reveals the morphology at different locations in the melt pools (Figure 1(b)). Note that the solidification morphology can be widely different across melt pool locations due to different local conditions; of which we present here only two snapshots for representation. Solidification grains with a cellular morphology is often observed that is sometimes difficult to distinguish between a transition morphology from planar to cellular or vice versa. We explore the variation of average composition measured across locations in the solidified grain morphology that is used as the 'ground truth' to compare with numerical simulations. Although not shown here, WDS measurements were used to estimate the composition variation in morphologies in which the composition profile was extracted as a function of solidification distance x (Figure 1(c)). The non-equilibrium microsegregation (k_v) was approximated from these profiles using

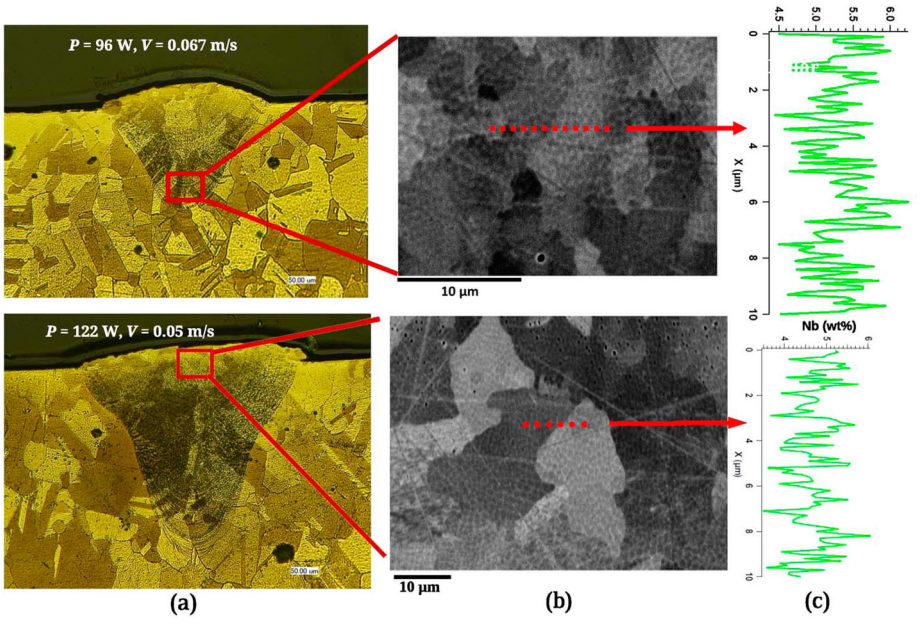

Figure 1. (Colour online) (a) Optical microscopy reveals the solidified Ni–Nb melt pools for different laser parameters. (b) The SEM analysis reveals the typical solidification grains at different locations in the solidified melt pool. Typical location-specific morphologies are cellular, planar, and (planar to cellular) transition that depend on the local G and V conditions in the molten pool. (c) The variation of Nb along the dotted lines is approximated from the corresponding WDS maps of the solidified morphologies.

a calculation of the *dimensionless* ratio of Nb in the solid (<5 wt%) and Nb in the liquid (>5 wt%), obeying steady-state solidification [15–18]. In all our experiments and analyses, k_v varied between 0.6 and 0.8 with a mean value of 0.72 and standard deviation of 0.1. A synthetic data set was created using these statistical metrics to compare with our simulation results. On average, our measurements of Nb microsegregation reasonably agree with other related LPBF experiments [26,28,44,45] conducted on Ni–Nb alloys.

3. Simulation details

We used a design-of-simulations approach to validate the k_v data approximated from the above LPBF experiments. An idealised multi-level FEA-PF simulation framework (Figure 2(a)) is employed. In particular, the forward approach is considered in this work to model the effects of inputs (say, X_i) on the output $Y = k_v$. Our 3D FEA thermal model [46,47] employed the standard implementation of heat transfer (including conduction, natural convection, radiation, and evaporation), boundary conditions, thermophysical properties, and process parameters. The FEA simulations were performed in COMSOL [48] heat transfer module for the varying values of laser power between 30 and 300 W and scan speed between

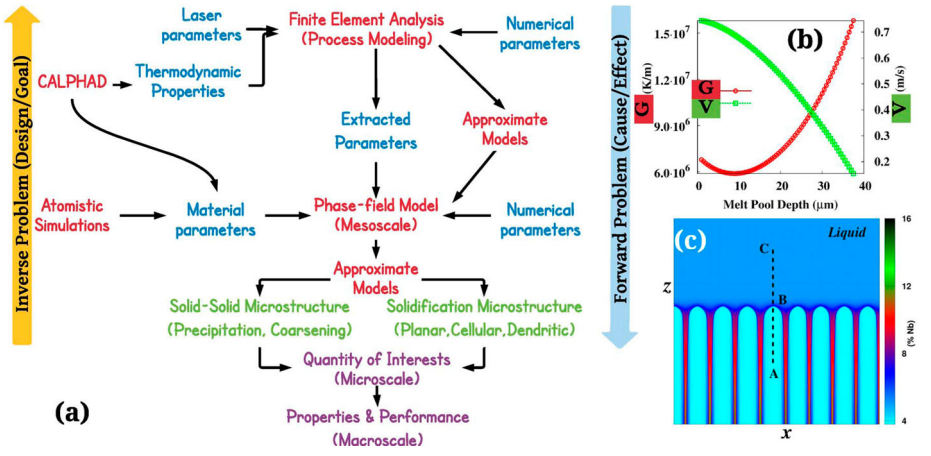

Figure 2. (Colour online) (a) A schematic of the overall simulation framework ('big picture') is illustrated. Red represents methods, and blue represents model inputs. The forward analysis propagates the effects of inputs onto output (k_v) in a top-down manner. A desired QoI in the bottom-level can be obtained after manipulating the parameters at the top-level in an inverse problem. Approximate models are statistical models. Although not considered here, material property inputs can be estimated from CALPHAD [51] and atomistic simulations [52] for realistic analysis. (b) The FEA simulations estimate G and V in the melt pool as a function of the solidification distance. (c) The values of G and V input to the PF model to simulate cellular morphology in which the microsegregation is determined and modelled using suitable statistical methods.

0.05 and 2.5 m s^{-1} that correspond to LPBF of Ni–Nb alloys. The solidification parameters – G and V – were extracted from the resulting melt pool liquidus isotherm as a function of the melt pool depth (Figure 2(b)), where G typically varied between 2×10^6 K m^{-1} to 5×10^7 K m^{-1} and V varied between 0.05 and 2.5 m s^{-1} for all the laser processing parameters employed. Next, a quantitative alloy PF solidification model [49] with zero anti-trapping solute flux was employed to simulate location-specific microstructures for the above values of G and V. Further details of the PF model equations, model parameters, and alloy parameters can be found in [47]. Ignoring curvature effects, k_v was determined from all our simulations following a Ni-rich cell along the line A–B–C (Figure 2(c)), using the dimensionless ratio of Nb at region A (cell core) and region B (cell tip). Although the k_v determined this way was used as a reference for our statistical analysis, for a more accurate estimation of k_v, the effect of cell tip curvature (ρ) on k_v by $k_v(1 - (1 - k_v)d_0/\rho$ (d_0 is chemical capillary length) can be included [18,50]. The value of k_v is unique along the cells during steady-state for a particular set of values of local conditions.

4. Statistical analysis

Parametric statistical methods are used in general to model the underlying relationship between X_i and k_v given by: $k_v = f(X_i) + \epsilon$, where f is some fixed

but unknown functions that approximate k_v and ε is a random error term. In this work, we explore several linear and non-linear forms of f for the prediction of k_v and inference between X_i and k_v. Linear or non-linear regression of k_v as a function of p inputs, X_i, where $i \in \{1, 2, \ldots, p\}$, is essential to model the sensitivity of inputs onto the variability in k_v [38,39]. The set X_i is chosen as $\{G, V, D, \Gamma, k\}$ (Figure 3), where the material parameters – D the diffusivity of liquid, Γ the Gibbs–Thomson coefficient (a cell-liquid surface tension related parameter), and k the equilibrium partition coefficient – are considered from the Ni–Nb phase diagram [53].

In our PF simulations, the values of X_i varied between predefined ranges (refer to Table 1 in Ref. [47]), resulting in (non-equilibrium) k_v values ranging between 0.7 and 0.9. These k_v values are plotted as a function of one of the predictors, k, in Figure 3(a). On average, the simulated k_v falls within the experimentally approximated k_v range ($0.6 \pm 0.1 < k_v < 0.8 \pm 0.1$). In order to model the statistical effects of X_i on k_v, the baseline approach is to fit the k_v data using a simple linear regression (SLR) model [38] of the following

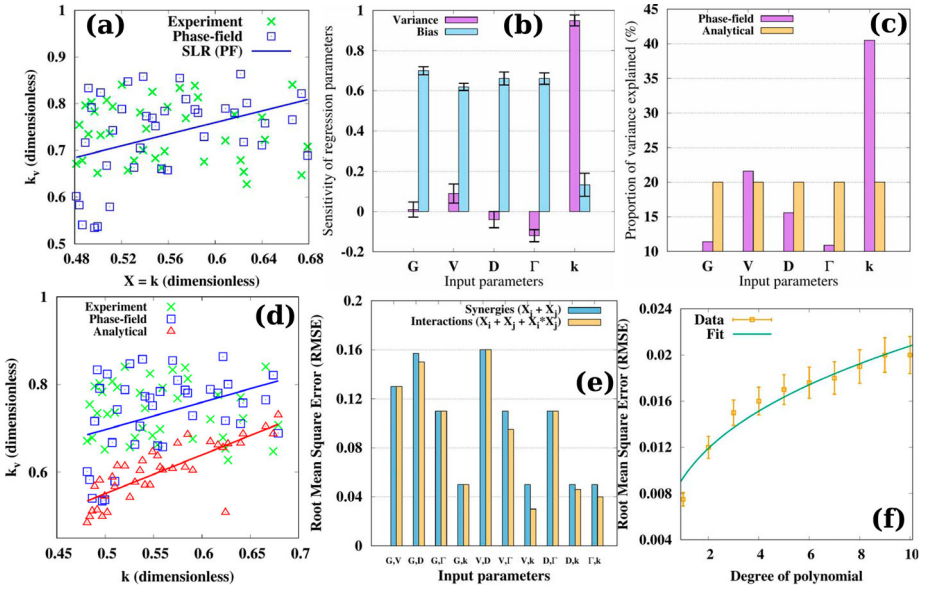

Figure 3. (Colour online) (a) A scatterplot represents the PF-simulated output k_v data as a function of the input predictor k. Such scatterplot representation for other predictors is not shown here. On average, the PF data fall within the experimental observed k_v range. The PF-simulated k_v data were fit using the SLR model (Equation (1)). (b) The sensitivity of the normalised SLR coefficients for each predictor, as for k in Figure 3(a), was determined using the standard deviation around the mean values of bias and variance. (c) The proportion of variance contributed by each predictor on k_v is calculated using PF and KF model predictions. (d) The $\mathbb{KL}$ and $\mathbb{HD}$ distances are small between experimental and PF data and are large between experimental and KF predictions. (e) Interactions between the predictors were found insignificant in the MLR model form (Equation (4)). (f) Accuracy of the MLR model decreased with the increasing degrees of polynomial regression.

form for each predictor i

$$k_v^s = \beta_0^i + \beta_i X_i + \epsilon_s, \tag{1}$$

where variance β_0 signifies the mean of k_v, bias β_i determines the linear relationship between k_v and X_i, and ϵ_s is the estimation error in the line of best (least-squares) fit that represents the data on the scatterplot between X_i and k_v (Figure 3(a)). The absolute difference between the original model (PF) and the approximate SLR model (say, for $X_i = k$) data sets of size N was estimated using the metric of root mean square error (RMSE) [54]: $\sqrt{(1/N)\sum_{i=1}^{N}[k_v(i) - k_v^s(i)]^2}$ = 0.19. The uncertainty associated during the estimation of β_0 and β_i for each X_i is shown as error bar in Figure 3(b). Maintaining a bias-variance trade-off [38,39] is essential for understanding the behaviour/error ($\propto$ bias^2 + variance) of the prediction models. This is primarily controlled here by V and D (Figure 3(b)), since their Pearson correlations with k_v are in the opposite direction [47]. An analysis of the proportion of variance contributed by X_i on k_v (Figure 3(c)) reveals that the effects of G and Γ are small, while the effects of V, D, and k are considerable, with the effect of k being the most significant in the AM limit. The high variance attributed by k on k_v can potentially be compensated via a high bias imposed by $\{G, V, D, \Gamma\}$. Therefore, each X_i was considered for statistical modelling of k_v.

A relatively large number (here, $N = 40$) of PF simulations and in turn data are needed for more accurate data analysis. However, PF simulations are computationally intensive, and hence, minimisation of the simulation time is essential. Therefore, as an alternative to PF simulations, we explore the predictive potential of the analytical KF model [18] to estimate k_v following

$$k_v^a = 1 - (1 - k)P\exp(P)E_1(P) + \epsilon_a, \tag{2}$$

where $E_1(P)$ is the first exponential integral of the interface Péclet number $P = f(G, V, D, \Gamma)$ [18]. The predictors in the KF model contribute equal variance on k_v, unlike the PF analysis (Figure 3(c)). While this can be intuitively true for the low-V solidification limit, it rarely applies in the high-V AM limit. Thus, the KF prediction is found to be 'statistically' far from both PF and experimental data sets (Figure 3(d)). Although not shown here, this was quantified using the asymmetric Kullback–Leibler [39] ($\mathbb{KL}$) and symmetric Hausdorff [55] ($\mathbb{HD}$) distance metrics between the involved data sets, resulting in ascending distance measures when compared between experimental measurements and each of PF and KF predictions.

As the KF model did not represent the AM solidification data well and in order to minimise repetitive PF calculations, a Gaussian process (GP) surrogate model of the form (refer to [47,56] for the details of mean m, covariance c,

correlation matrix Σ, and hyperparameter $\mathbf{\Phi}$ functions),

$$k_v^g \mid \mathbf{\Phi} \sim \mathcal{GP}\big(m(\boldsymbol{X}_i, k_v), c(\boldsymbol{X}_i, k_v), \boldsymbol{\Sigma}\big) + \epsilon_g, \tag{3}$$

was used to approximate the PF data set (Figure 4(a)). This led to significant gain in run time, and the GP prediction lied at a 'statistically' smaller distance to the experimental data when compared to the KF prediction. Although the GP model may seem computationally inexpensive on the surface, it still requires the parent PF k_v data for training [56,57]. This leads to the GP a less interpretable model for which inference is more challenging and thus less attractive from engineering perspective. Alternative statistical models are therefore necessary for a reasonably accurate yet interpretable prediction of k_v.

As an alternate heuristic approach, multiple least-squares regression (MLR) [38,39] was used as a baseline to model k_v, which is given by

$$k_v^m = \beta_0 + \sum_{i=1}^{p} \beta_i^d X_i^d + \sum_{i=1}^{p} \sum_{j \neq i}^{p-1} \beta_{ij} X_i^d X_j^d + \epsilon_m, \tag{4}$$

where β_i are the coefficients, X_i the predictors, and d the degree of polynomial. In such a generalised additive model (GAM) form [38], each X_i contributes through synergies ($\sum X_i$) and interactions ($\sum_{i \neq j} X_i X_j$). Although not shown here, a linear combination of synergies with d=1 reduces the variance of k_v significantly. When the binary and higher order interactions among X_i were considered, the accuracy of the MLR model decreased with the increasing values of d (Figure 3(e,f)). Therefore, the most efficient MLR model was found to be of the form: $k_v^m = \beta_0 + \beta_G G + \beta_V V + \beta_D D + \beta_\Gamma \Gamma + \beta_k k$ with RMSE = 0.09. We wish to note that the KF model (Equation (2)) can also be expressed in the above MLR form for the sake of generality and without much loss of accuracy

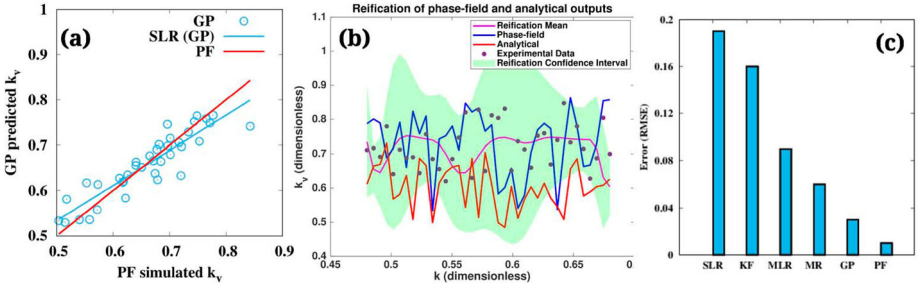

Figure 4. (Colour online) (a) A GP surrogate model (Equation (3)) is used to approximate the PF-simulated k_v data. On average, the GP prediction closely follows the PF data (RMSE = 0.03). (b) Information fusion of the PF and KF data sets was employed following Equation (5) to derive a more accurate prediction of k_v. Since the experimental data showed relatively good agreement with the high-fidelity PF model prediction, the reified mean is attracted toward the PF data. Overall, as a reference to the experimental data, the MR prediction has lower RMSE (=0.06) compared to MLR forms of PF (RMSE = 0.09) and KF (RMSE = 0.16). The reified mean is presented along with the 95% confidence interval, which, on average, captures all experimental data points. (c) The accuracy of various numerical models is compared with reference to the ground truth.

(RMSE = 0.16). Since our MLR data sets lie on a 5-D hyperplane, which is difficult to visualise, it is not shown here.

With an aim to derive a more accurate statistical model to predict k_v, the MLR forms of PF and KF models (or, the model data sets) were combined together using a recent model reification (MR) approach,

$$k_v^f = c_1 k_v^a + c_2 k_v^m + \epsilon_f, \tag{5}$$

where c_1 and c_2 are constants estimated *via* machine learning. MR is an information source fusion methodology that elevates each available information source k_v^a (Equation (2)) and k_v^m (Equation (4)) to the role of 'ground truth' in turn so as to enable the estimation of correlations between the discrepancies of each information source from actual ground truth. This process, detailed in [43], when implemented in MATLAB [58] provides a fused information source (Figure 4(b)) with lower variance and bias from any of its constituent sources. Thus, depending on the model sources, MR approach can potentially lead to the best representation of k_v.

5. Summary and outlook

We reviewed suitable statistical models to represent microsegregation that was estimated by LPBF experiments and validated by FEA-PF simulations. The prediction accuracy or flexibility of these models decreased following GP, MR, MLR, KF, and SLR, while the model interpretability increased in the reverse order (Figure 4(c)). Our work can be further improved in the following key directions. Prediction accuracy and model interpretability can potentially be improved when the least-squares fit applied to the data for a reduced number of predictors that are determined after suitable subset selection, regularisation, and dimensional reduction techniques [38]. Fully non-linear ML methods such as bagging, boosting, and random forest may yield a more accurate prediction of k_v, although at the expense of less interpretability for which inference is even more challenging [38,39]. Suitable ML approaches such as compressed-sensing are necessary to assess the performance of the above models for a given data set and size [59]. Finally, for improved quantitative analysis, a large number of observations are needed. In this way, a statistical basis for AM microstructural features extraction and interpretation can be established toward rapid engineering decision and policy-making, which will help to identify nominal in-process microstructure-property space of the AM metal alloy for which overall processing time and cost are optimal.

Acknowledgments

We thank the support of the National Science Foundation Grants: CMMI-1534534, CMMI-1663130, and DGE-1545403. High-throughput FEA and PF simulations were carried out at

the Ada and Terra Texas A&M University supercomputing facilities. S.G. thanks L. Johnson and M. Mahmoudi for useful discussions.

Disclosure statement

No potential conflict of interest was reported by the author(s).

Funding

We thank the support of the National Science Foundation [grants numbers CMMI-1534534, CMMI-1663130, and DGE-1545403].

ORCID

Supriyo Ghosh http://orcid.org/0000-0001-7265-5266
Ibrahim Karaman http://orcid.org/0000-0001-6461-4958
Raymundo Arroyave http://orcid.org/0000-0001-7548-8686

References

[1] D. Herzog, V. Seyda, E. Wycisk and C. Emmelmann, Acta Mater. 117 (2016) p.371.
[2] L.E. Murr, E. Martinez, K.N. Amato, S.M. Gaytan, J. Hernandez, D.A. Ramirez, P.W. Shindo, F. Medina and R.B. Wicker, J. Mater. Res. Technol. 1 (2012) p.42.
[3] W.J. Sames, F.A. List, S. Pannala, R.R. Dehoff and S.S. Babu, Int. Mater. Rev. 61 (2016) p.315.
[4] W.E. Frazier, J. Mater. Eng. Perform. 23 (2014) p.1917.
[5] T. DebRoy, H. Wei, J. Zuback, T. Mukherjee, J. Elmer, J. Milewski, A. Beese, A. Wilson-Heid, A. De and W. Zhang, Prog. Mater. Sci. 92 (2018) p.112.
[6] S. Gorsse, C. Hutchinson, M. Gouné and R. Banerjee, Sci. Technol. Adv. Mater. 18 (2017) p.584.
[7] T.D. Ngo, A. Kashani, G. Imbalzano, K.T. Nguyen and D. Hui, Compos. B. Eng. 143 (2018) p.172.
[8] J.J. Lewandowski and M. Seifi, Annu. Rev. Mater. Res. 46 (2016) p.151.
[9] D. Bourell, J.P. Kruth, M. Leu, G. Levy, D. Rosen, A.M. Beese and A. Clare, CIRP Ann. 66 (2017) p.659.
[10] N. Shamsaei, A. Yadollahi, L. Bian and S.M. Thompson, Addit. Manuf. 8 (2015) p.12.
[11] M. Seifi, A. Salem, J. Beuth, O. Harrysson and J.J. Lewandowski, JOM 68 (2016) p.747.
[12] W.E. King, A.T. Anderson, R.M. Ferencz, N.E. Hodge, C. Kamath, S.A. Khairallah and A.M. Rubenchik, Appl. Phys. Rev. 2 (2015) p.041304.
[13] M.M. Attallah, R. Jennings, X. Wang and L.N. Carter, MRS Bull. 41 (2016) p.758.
[14] S.S. Babu, N. Raghavan, J. Raplee, S.J. Foster, C. Frederick, M. Haines, R. Dinwiddie, M. Kirka, A. Plotkowski, Y. Lee and R.R. Dehoff, Metall. Mater. Trans. A 49 (2018) p.3764.
[15] S. Ghosh, L. Ma, N. Ofori-Opoku and J.E. Guyer, Model. Simul. Mater. Sci. Eng. 25 (2017) p.065002.
[16] A. Farzadi, M. Do-Quang, S. Serajzadeh, A.H. Kokabi and G. Amberg, Model. Simul. Mater. Sci. Eng. 16 (2008) p.065005.
[17] W. Kurz and D.J. Fisher, *Fundamentals of Solidification*, Trans Tech Publications, Zurich, 1998.

[18] M. Rappaz and J.A. Dantzig, *Solidification, Engineering Sciences*, EFPL Press, Lausanne, 2009.
[19] R.C. Reed, *The Superalloys: Fundamentals and Applications*, Cambridge University Press, Cambridge, 2008.
[20] G.A. Knorovsky, M.J. Cieslak, T.J. Headley, A.D. Romig and W.F. Hammetter, Metall. Trans. A 20 (1989) p.2149.
[21] T. Keller, G. Lindwall, S. Ghosh, L. Ma, B. Lane, F. Zhang, U.R. Kattner, E.A. Lass, J.C. Heigel, Y. Idell, M.E. Williams, A.J. Allen, J.E. Guyer and L.E. Levine, Acta Mater. 139 (2017) p.244.
[22] S. Ghosh, Mater. Res. Express 5 (2018) p.012001.
[23] Y.J. Liang, X. Cheng and H.M. Wang, Acta Mater. 118 (2016) p.17.
[24] K. Karayagiz, L. Johnson, R. Seede, V. Attari, B. Zhang, X. Huang, S. Ghosh, T. Duong, I. Karaman, A. Elwany and R. Arróyave, Acta Mater. 185 (2020) p.320.
[25] J. Kundin, L. Mushongera and H. Emmerich, Acta Mater. 95 (2015) p.343.
[26] R. Acharya, J.A. Sharon and A. Staroselsky, Acta Mater. 124 (2017) p.360.
[27] M. Francois, A. Sun, W. King, N. Henson, D. Tourret, C. Bronkhorst, N. Carlson, C. Newman, T. Haut, J. Bakosi, J. Gibbs, V. Livescu, S.V. Wiel, A. Clarke, M. Schraad, T. Blacker, H. Lim, T. Rodgers, S. Owen, F. Abdeljawad, J. Madison, A. Anderson, J.-L. Fattebert, R. Ferencz, N. Hodge, S. Khairallah and O. Walton, Curr. Opin. Solid State Mater. Sci. 21 (2017) p.198.
[28] X. Wang, P. Liu, Y. Ji, Y. Liu, M. Horstemeyer and L. Chen, J. Mater. Eng. Perform. 28 (2019) p.657.
[29] L.-X. Lu, N. Sridhar and Y.-W. Zhang, Acta Mater. 144 (2018) p.801.
[30] W.J. Boettinger, J.A. Warren, C. Beckermann and A. Karma, Annu. Rev. Mater. Res. 32 (2002) p.163.
[31] L.Q. Chen, Annu. Rev. Mater. Res. 32 (2002) p.113.
[32] N. Moelans, B. Blanpain and P. Wollants, Calphad 32 (2008) p.268.
[33] I. Steinbach, Model. Simul. Mater. Sci. Eng. 17 (2009) p.073001.
[34] S. Ghosh, N. Ofori-Opoku and J.E. Guyer, Comput. Mater. Sci. 144 (2018) p.256.
[35] X. Wang, P. Liu, Y. Ji, Y. Liu, M. Horstemeyer and L. Chen, J. Mater. Eng. Perform. 28 (2019) p.657.
[36] K.T. Butler, D.W. Davies, H. Cartwright, O. Isayev and A. Walsh, Nature 559 (2018) p.547.
[37] Y. Liu, T. Zhao, W. Ju and S. Shi, J. Materiomics 3 (2017) p.159.
[38] G. James, D. Witten, T. Hastie and R. Tibshirani, *An Introduction to Statistical Learning*, Springer, New York, 2013.
[39] K. Murphy and F. Bach, *Machine Learning: A Probabilistic Perspective*, MIT Press, Cambridge, MA, 2012.
[40] Z. Hu and S. Mahadevan, Int. J. Adv. Manuf. Technol. 93 (2017) p.2855.
[41] F. Lopez, P. Witherell and B. Lane, J. Mech. Des. 138 (2016) p.114502.
[42] G. Tapia, W. King, L. Johnson, R. Arroyave, I. Karaman and A. Elwany, J. Manuf. Sci. Eng. 140 (2018) p.121006.
[43] W.D. Thomison and D.L. Allaire, A model reification approach to fusing information from multifidelity information sources, in *19th AIAA Non-Deterministic Approaches Conference*, Grapevine, TX, (2017) p. 1949.
[44] Y. Tian, J. Muñiz-Lerma and M. Brochu, Mater. Charact. 131 (2017) p.306.
[45] P. Tao, H. Li, B. Huang, Q. Hu, S. Gong and Q. Xu, Vacuum 159 (2019) p.382.
[46] K. Karayagiz, A. Elwany, G. Tapia, B. Franco, L. Johnson, J. Ma, I. Karaman and R. Arroyave, IISE Trans. 51 (2018) p.136.

[47] S. Ghosh, M. Mahmoudi, L. Johnson, A. Elwany, R. Arroyave and D. Allaire, Model. Simul. Mater. Sci. Eng. 27 (2019) p.034002.
[48] COMSOL, Multiphysics reference guide for COMSOL 4.2, 2011.
[49] B. Echebarria, R. Folch, A. Karma and M. Plapp, Phys. Rev. E 70 (2004) p.061604.
[50] A.M. Mullins, J. Rosam and P.K. Jimack, J. Cryst. Growth. 312 (2010) p.1891.
[51] J.-O. Andersson, T. Helander, L. Höglund, P. Shi and B. Sundman, Calphad 26 (2002) p.273.
[52] J. Hoyt, M. Asta and A. Karma, Mater. Sci. Eng. R: Rep. 41 (2003) p.121.
[53] J. Davis and A. Committee, *Nickel, Cobalt, and Their Alloys, ASM Specialty Handbook*, ASM Int., Materials Park, OH, 2000.
[54] D. Montgomery and G. Runger, *Applied Statistics and Probability for Engineers*, Wiley, Hoboken, NJ, 2014.
[55] Y. Gao and Q. Dai, *View-based 3-D Object Retrieval*, Elsevier Science, Amsterdam, 2014.
[56] M. Mahmoudi, G. Tapia, K. Karayagiz, B. Franco, J. Ma, R. Arroyave, I. Karaman and A. Elwany, Integr. Mater. Manuf. Innov. 7 (2018) p.116.
[57] C. Rasmussen and C. Williams, *Gaussian Processes for Machine Learning*, MIT Press, Cambridge, MA, 2006.
[58] MATLAB, *Version R2018a*, The MathWorks Inc., Natick, MA, 2018.
[59] R. Ouyang, S. Curtarolo, E. Ahmetcik, M. Scheffler and L. Ghiringhelli, Phys. Rev. Mater. 2 (2018) p.083802.